Predicting High-Speed Machining Dynamics by Substructure Analysis

T. L. Schmitz
National Institute of Standards and Technology, Automated Production Technology Division, Gaithersburg, USA
Submitted by R. R. Donalson (1), Pleasanton, USA
Received on January 4, 2000

Abstract

The practical implementation of high-speed machining (HSM) requires accurate knowledge of the machine dynamics. We apply receptance coupling substructure analysis to the prediction of the tool point dynamic response, combining frequency response measurements of individual components through appropriate connections to determine assembly dynamics using simple vector manipulations. This paper shows that the dynamic response before and after system changes may be predicted, thus dramatically reducing the number of required experimental measurements. The application of this technique to the tuning of tool dynamics for improved stability by overhung length variation is demonstrated.

Keywords: High speed machining, Sub-structure analysis

1 INTRODUCTION

Much recent research has focused on high-speed machining (HSM) techniques [e.g., 1-12]. Both the implementation of HSM and the accurate simulation of the forces and deflections during machining under high speed conditions have been explored. Implementation techniques have considered the system dynamics, self-excited vibration theory for the calculation of stability lobes, machine/spindle design requirements, and sensors capable of chatter recognition. HSM simulations have included numerical time-domain methods and analytical solutions for the nonlinear, quasi-periodic regenerative process stability [3,4,8,13-16]. In all cases, one of two positions was taken with respect to the system dynamics: 1) the dynamics of the tool/workpiece/machine are considered fixed and the machining conditions are selected according to the experimental or computed tool point dynamics, and 2) the tool point dynamics are adjusted by varying the tool length to make use of local increases in the process stability (*tool tuning*) [2,8,32].

The well-known stability lobe diagram, which predicts system stability as a function of spindle speed and machining parameters, is commonly used in HSM development (see Figure 1). Stable and unstable regions are seen depending on the selected spindle speed and axial depth of cut, b. Two approaches may be taken in producing this diagram. An analytical solution may be selected (e.g., [15,17-20]) or time-domain techniques may be used [3,9,13,14]. In either case, knowledge of the system dynamics *reflected at the tool point* is required. In most cases, the dynamics are obtained using impact testing and modal analysis. The direct (or driving point) frequency response function (FRF) is measured at the tool tip (only) and a fit to the experimental data is performed. The modal parameters (i.e., mass, m, stiffness, k, and damping ratio, ζ) are extracted from each dominant mode and these values are used as input to the analytical or time-domain simulations [3,8,13,14,21,22, 30]. Other possibilities include computational methods for modal parameter determination and milling experiments for direct stable speed selection [1]. In all cases, however, the measurements are specific to the selected components (e.g., tool length and geometry, tool holder, workpiece, spindle, and machine) and boundary conditions (e.g., holder force and drawbar force [23]).

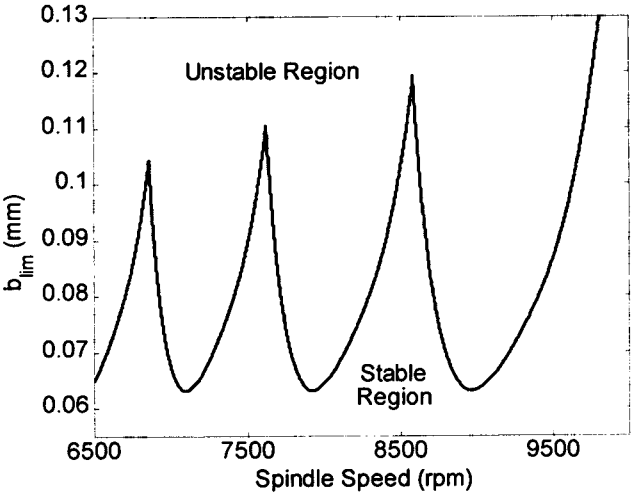

Figure 1: Example Stability Lobe Diagram.

To fully exploit the increased manufacturing efficiency associated with HSM, it is important to: 1) predict tool point dynamics without the measurement of each new tool/holder/spindle combination, and 2) provide repeatable and robust dynamic responses between machines, holders, and setups. This paper uses receptance coupling substructure analysis to address the former. It is demonstrated on a specific industrially motivated, *tool tuning* example where the capability of FRF prediction dramatically reduced the number of FRF measurements necessary to select an appropriate tool length for optimized stability.

2 SUBSTRUCTURE ANALYSIS

In receptance coupling substructure analysis, experimental or analytic FRFs for the individual components are used to predict the final assembly's

dynamic response at any spatial coordinate selected for component measurements [24-27]. Experimental FRFs are required only at the coordinate of interest (tool point) and any connection coordinates. Contrary to modal coupling and finite element methods, the number of modeled structural modes in each component does not define the number of required measurement locations and knowledge of the mode shapes of each component is not required. Furthermore, no matrix inversions are necessary, only vector manipulations.

2.1 Receptance Coupling

A receptance coupling example will now be given (see Figure 2). The two components, *A* and *B*, are to be connected at spatial coordinates x_2 and x_3 through the linear spring, k_x, to give the assembly, *C*. The direct FRF at coordinate X_1 of the assembly is desired.

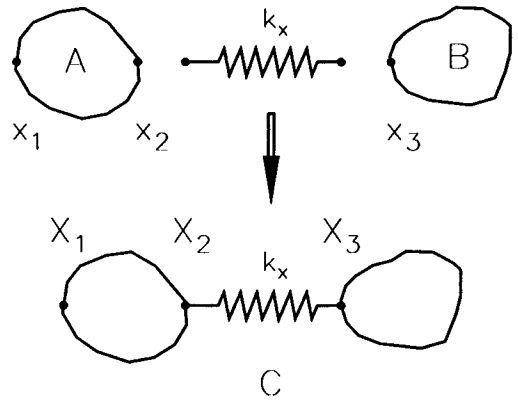

Figure 2: Receptance Coupling Model.

The receptance matrix, $G(\omega)$, which relates the complex displacement at each assembly coordinate to harmonic input forces for the assembled system, is derived using the receptance coupling method [25]. This 3x3 matrix (for the three degree of freedom system) is calculated by columns. The first column is determined by applying a force, F_1, to coordinate X_1. Figure 3 displays the assembled and component systems with F_1 applied to the assembled system.

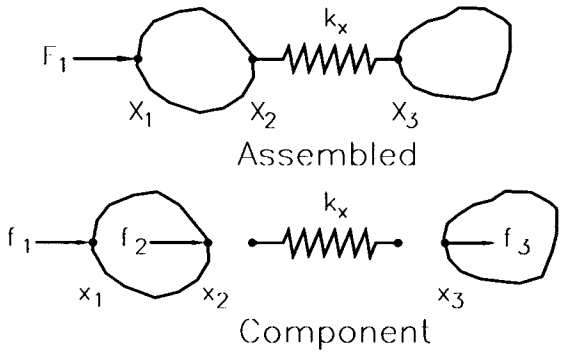

Figure 3: Receptance Matrix Column 1 Determination.

Considering the component system in Figure 3, the displacements at the three coordinates may be written as shown in Equation 1. The notation *H* refers to the spatial receptance matrices of the individual components before assembly, with subscripts, *ij*, that refer to the measurement and forcing locations, respectively. The equilibrium and compatibility conditions for the components are given in Equations 2 and 3.

$$\begin{aligned} x_1 &= H_{11}f_1 + H_{12}f_2 \\ x_2 &= H_{21}f_1 + H_{22}f_2 \\ x_3 &= H_{33}f_3 \end{aligned} \qquad \text{Displacements} \qquad (1)$$

$$\begin{aligned} f_1 &= F_1 \\ f_2 + f_3 &= 0 \end{aligned} \qquad \text{Equilibrium Conditions} \qquad (2)$$

$$\begin{aligned} x_i &= X_i \\ x_3 - x_2 &= \frac{-f_3}{k_x} \end{aligned} \qquad \text{Compatibility Conditions} \qquad (3)$$

Substituting Equations 1 and 2 into Equation 3 leads to the expressions for $G_{11}(\omega)$, $G_{21}(\omega)$, and $G_{31}(\omega)$. Equation 4 shows $G_{11}(\omega)$, the direct FRF at coordinate X_1 of the assembly.

$$G_{11}(\omega) = \frac{X_1}{F_1} = H_{11} - H_{12}\left(H_{33} + H_{22} + \frac{1}{k_x}\right)^{-1} H_{21} \qquad (4)$$

This example is analogous to tool point FRF prediction. Component *A* (the tool) is attached to component *B* (the holder and spindle) through experimentally determined or predicted connection springs/dampers and the direct FRF at X_1 (the cantilever end of the tool) is desired for stability prediction and chatter free machining parameter selection.

2.2 Free-Free Tool FRFs

In the previous example, free-free state (or unsupported) FRFs of component *A* (the tool) were required (H_{11}, H_{12}, H_{21}, and H_{22}). For these measurements, the tool is unrestrained (degenerate) and rigid body, zero frequency modes are present, as well as the expected vibratory response [28]. There are several difficulties associated with obtaining these FRFs using impact testing: 1) the free-free state is difficult to realize in practice, 2) low mass, wide bandwidth accelerometers typically do not perform well at low frequencies, and 3) the response for low mass tools is easily corrupted by the accelerometer mass.

The analytic formulation for free-free tool FRFs was therefore developed to replace the experimental measurements. These analytic forms for the tool's direct and cross FRFs are then used in the receptance coupling method.

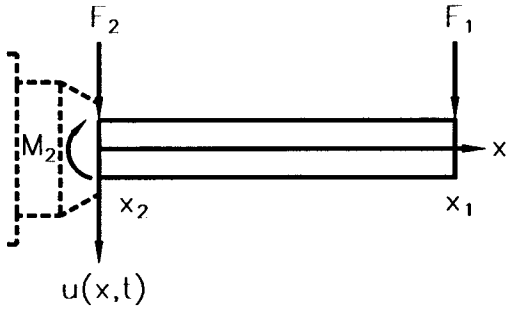

Figure 4: Tool Loading Conditions.

Figure 4 shows the loads applied to the tool when connected to the holder/spindle. A force is applied to the free end (x_1) while the end to be inserted in the holder (x_2) opposes displacement and rotation (i.e., a cantilever beam). The equation of motion for this model is shown in Equation 5. Here, $u(x,t)$ is the temporal displacement at any point along the beam and $q(x,t)$ is the externally applied loads. Additionally, ρ is the beam mass per unit length, c' is the viscous damping coefficient per unit length, *E* is Young's modulus (homogeneity assumed), and *I* is the second area moment of inertia (uniform cylindrical cross-section assumed).

$$\rho\frac{\partial^2 u(x,t)}{\partial t^2} + c'\frac{\partial u(x,t)}{\partial t} + EI\frac{\partial^4 u(x,t)}{\partial x^4} = q(x,t) \qquad (5)$$

If harmonic motion is assumed, a solution for the lateral vibration of the beam at any coordinate along its length (L) may be obtained from Equation 5 for each beam mode. These results are then summed to determine the total vibration at that location.

In this analysis, two rigid body modes (inertial translation and rotation about the center of mass) were summed with analytic expressions for the beam free-free modes [29] to determine the tool vibration. Expressions for the direct FRFs at coordinates x_1 and x_2 (H_{11} and H_{22}, respectively) and a cross FRF H_{12} (H_{21} is equivalent by reciprocity) are shown in Equation 6, where λ_i is a dimensionless frequency parameter [29].

The receptance term H_{11}, for example, contains three components. The first two represent the contributions by the translational and rotational rigid body modes, respectively, while the third gives the response due to the free-free modes ($\phi_i(x)$, expressed as shown in Equation 7) which have been evaluated at coordinate x_1 (a distance L from the model origin). Response functions that relate displacement to applied moment (L_{ij}), rotation to applied force (N_{ij}), and rotation to applied moment (P_{ij}) were also derived.

$$H_{11}(\omega)=\frac{1}{-\rho L\omega^2}+\frac{3}{-\rho L\omega^2}+\sum_{i=1}^{\infty}\frac{\varphi_i(L)^2}{-\rho L\omega^2+ic'L\omega+\frac{EI\lambda_i^4}{L^3}}$$

$$H_{22}(\omega)=\frac{1}{-\rho L\omega^2}+\frac{3}{-\rho L\omega^2}+\sum_{i=1}^{\infty}\frac{\varphi_i(0)^2}{-\rho L\omega^2+ic'L\omega+\frac{EI\lambda_i^4}{L^3}}$$

$$H_{12}(\omega)=\frac{1}{-\rho L\omega^2}-\frac{3}{-\rho L\omega^2}+\sum_{i=1}^{\infty}\frac{\varphi_i(L)\varphi_i(0)}{-\rho L\omega^2+ic'L\omega+\frac{EI\lambda_i^4}{L^3}} \quad (6)$$

$$\varphi_i(x)=\cosh\frac{\lambda_i x}{L}+\cos\frac{\lambda_i x}{L}-\sigma_i\left(\sinh\frac{\lambda_i x}{L}+\sin\frac{\lambda_i x}{L}\right) \quad (7)$$

$$\sigma_i=\frac{\cosh\lambda_i-\cos\lambda_i}{\sinh\lambda_i-\sin\lambda_i}$$

The validity of this modeling strategy was tested in simulation. The free-free beam analytic model was attached to ground through infinitely stiff linear and rotational springs to verify that the assembly response at the free end approached that of a cantilever beam. It was determined that many free-free modes were necessary to adequately model the cantilever response. In Figure 5, the variation in the predicted natural frequency for a 19.1 mm diameter, 152.4 mm long aluminum shaft as a function of the number of included modes is shown. It is seen that approximately 86 modes are necessary to predict a value within 1% of the analytically predicted cantilever frequency of 578.6 Hz (shown as the dashed line in Figure 5). This large number of required modes for accurate frequency prediction precludes the use of experimental techniques to obtain the free-free tool response (due to limited measurement bandwidth), but is well suited to analytic predictions.

3 EXPERIMENTAL METHOD

To verify the receptance coupling technique and provide an example of *tool tuning* to optimize machining stability, three long, slender tools (length to diameter ratios of 8:1, 9:1, and 10:1) were selected for use in a horizontal spindle high-speed machining center. The tungsten carbide (cobalt binder) tools had two flutes and a relieved diameter of 11.8 mm for the portion of the tool outside the holder (12.7 mm inside). This tooling had previously been examined for machining of an aluminum part with 102 mm deep, 38 mm wide hexagonal pockets with 0.5 mm wall thickness [8]. Empirically determined, improved stability was reported for a 10:1 length/diameter ratio.

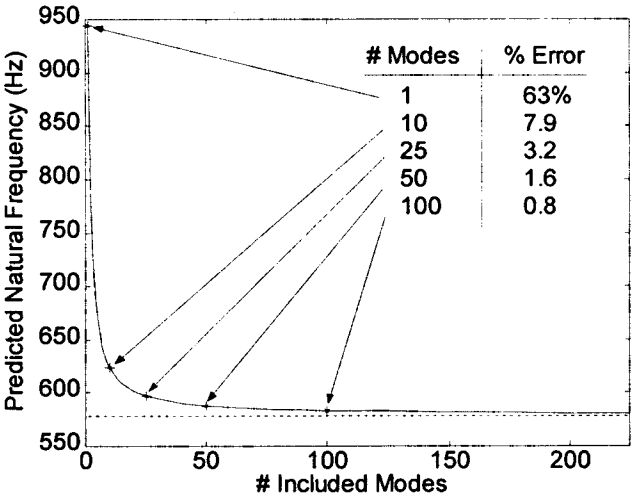

Figure 5: Cantilever Response Convergence.

3.1 Component Dynamic Characterization

The first step in predicting the assembled system's tool point response is to determine the component responses. As shown in the example in Section 2.1, for component B (the holder/spindle combination) only the direct FRFs at the connection coordinate (H_{33}, L_{33}, N_{33}, and P_{33}) are required. The direct FRF H_{33} was obtained by impact testing. A low mass, wide bandwidth accelerometer was placed at the free end of the collet holder and this location excited by a modally tuned impact hammer for both the X and Y coordinate directions. The result and a nine mode fit to the Y direction experimental data is shown in Figure 6. The remaining FRFs (pertaining to moment and rotation) were assumed zero.

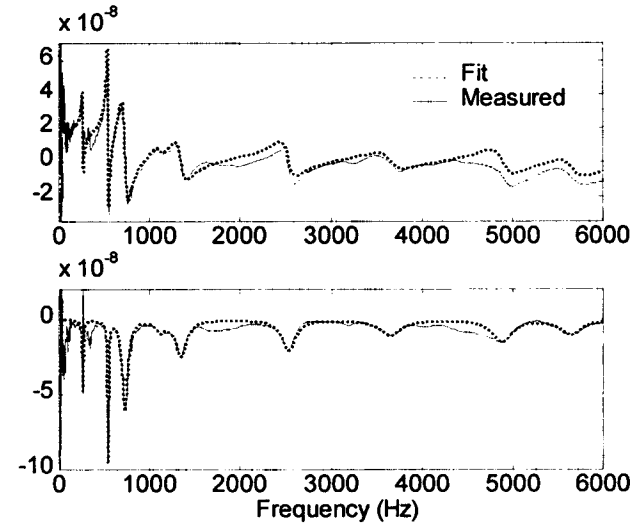

Figure 6: Holder/Spindle Y Direction Direct FRF (H_{33}).

The required tool FRFs were derived analytically (Section 2.2). Impact testing on the tools was performed to experimentally estimate Young's modulus and the viscous damping ratio of the tool material. These values, as well as the nominal tool dimensions, were then substituted in the analytic FRF terms.

3.2 Receptance Coupling

The receptance coupling formulation was composed of two parts. First, the section of the tool inside the collet was connected to the holder/spindle assembly. Next, the overhung portion of the tool was joined with the previous result through linear and rotational springs and dampers. The model for the latter is shown in Figure 7.

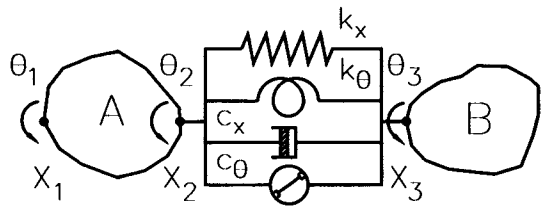

Figure 7: Tool/Holder/Spindle Assembly Model.

The receptance coupling derivation for the tool point direct FRF, $G_{11}(\omega)$, is similar to the example in 2.1, except there are now six degrees of freedom and damping is included. The displacements, equilibrium conditions, and compatibility conditions are determined from the system model and combined to calculate the assembly FRFs. The result for G_{11} is shown in Equation 8, where the H'_{ij}, L'_{ij}, N'_{ij}, and P'_{ij} terms represent mobility FRFs [22], or the ratio of linear or rotational velocity to force or moment. The linear and rotational stiffness and damping terms are labeled k_x, k_θ, c_x, and c_θ, respectively.

$$G_{11} = H_{11} - H_{12}E_1^{-1}E_2 - L_{12}E_3^{-1}\left(\left(k_\theta N_{21} + c_\theta N'_{21}\right) - E_4E_1^{-1}E_2\right)$$

where (8)

$$E_1 = \left(k_xH_{33} + k_xH_{22} + c_xH'_{33} + c_xH'_{22} + [1]\right) - E_3^{-1}E_4$$

$$\left(k_xL_{33} + k_xL_{22} + c_xL'_{33} + c_xL'_{22}\right)$$

$$E_2 = \left(k_xH_{21} + c_xH'_{21}\right) - E_3^{-1}\left(k_\theta N_{21} + c_\theta N'_{21}\right)$$

$$\left(k_xL_{33} + k_xL_{22} + c_xL'_{33} + c_xL'_{22}\right)$$

$$E_3 = \left(k_\theta P_{33} + k_\theta P_{22} + c_\theta P'_{33} + c_\theta P'_{22} + [1]\right)$$

$$E_4 = \left(k_\theta N_{33} + k_\theta N_{22} + c_\theta N'_{33} + c_\theta N'_{22}\right)$$

The analytic direct and cross FRFs for the tool and experimental modal fit to the holder/spindle direct FRF were then inserted in Equation 8 and the tool point dynamic response predicted. Experimental impact tests were also performed for each of the three selected tools. A comparison of the results is given in the next section.

4 RESULTS

Figures 8-10 show the experimental and predicted, Y direction tool point FRFs (G_{11}) for length to diameter ratios of 8:1, 9:1, and 10:1, respectively (note changes in vertical scales). The overall agreement between the predicted and measured results is good. However, small deviations are also seen. This is attributed to variations in collet torque between the three tool setups, imperfect knowledge of tool length/geometry, inaccurate fit to the holder/spindle FRF, and finite repeatability of the FRF measurement process.

The transition from the 8:1 to 9:1 case results in the anticipated decrease in both natural frequency and stiffness. For the 10:1 tool, however, the single tool mode seen in the two previous results has been effectively split into two dynamically stiffer modes, providing an increase in stability. This is due to interaction of the cantilever tool mode with the approximately 727 Hz Y direction holder/spindle mode (shown in Figure 6). The analog to this situation is the dynamic absorber, where a small spring/mass is added to a larger vibrating system. The spring constant and mass of the added system are selected such that the natural frequency is equal to the excitation frequency of the larger structure and the vibration of the support structure is reduced, theoretically, to zero at the driving frequency.

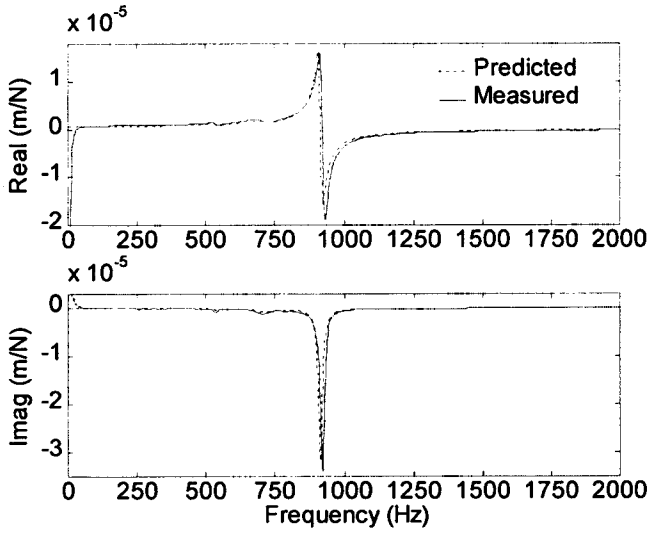

Figure 8: Experimental/Predicted FRF 8:1 Tool.

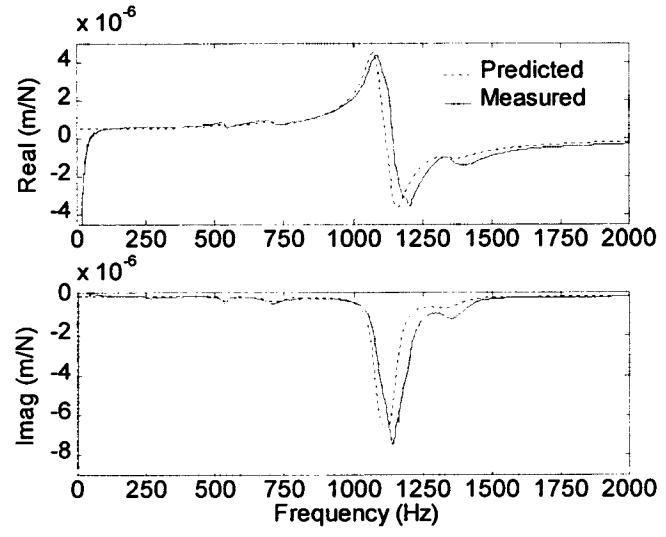

Figure 9: Experimental/Predicted FRF 9:1 Tool.

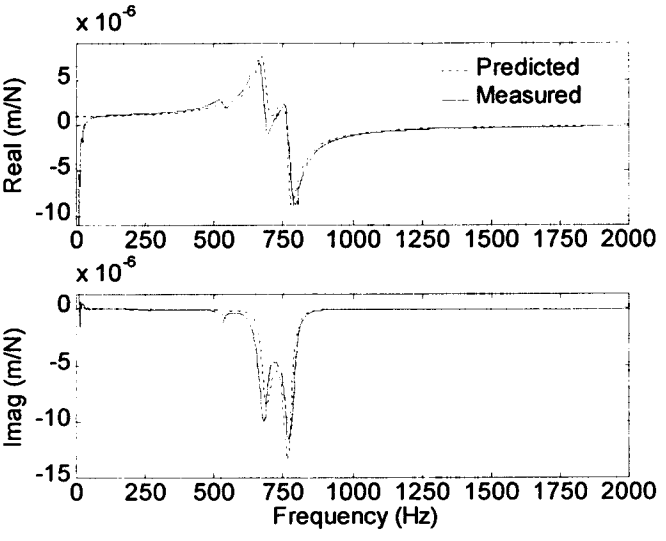

Figure 10: Experimental/Predicted FRF 10:1 Tool.

The selected linear and rotational spring and damping coefficients for the Y direction collet connection between the tool and holder/spindle for the three cases shown in Figures 8-10 are given in Table 1. It is anticipated that the system measured here (HSK 63A collet-type holder) represents a typical physical arrangement and, in general, a single set of values (with some associated uncertainty) may be used to represent the connection stiffness and damping for a particular holder. These values could be obtained in a single experimental setup (or determined from accurate modeling) and used for any tool/holder combination.

k_x (N/m)	k_θ (N-m/rad)	c_x(N-s/m)	c_θ (N-m-s/rad)
2.1×10^7	1.4×10^6	130	35

Table 1: Stiffness/Damping Coefficients.

5 DISCUSSION

Figures 8-10 show that interaction between tool and holder/spindle modes can dramatically affect the tool point FRF. To illustrate the effect of this interaction on machining performance, stability lobe diagrams for slotting cuts in the machine Y direction have been developed for the 9 and 10:1 tools. These are shown in Figures 11-12. It is seen that the 10:1 cutter offers a significantly higher critical stability limit (maximum stable axial depth of cut at all spindle speeds) than the 9:1 cutter, as well as a shift in the location of the stability lobes. This implies two possible optimization parameters: 1) tool length selection for interaction with holder/spindle modes to increase the local stability limit, and 2) tool length selection to move a highly stable lobe to the top spindle speed of the machine (e.g., for a top spindle speed of 20000 rpm, the 10:1 tool would be selected) [2,32].

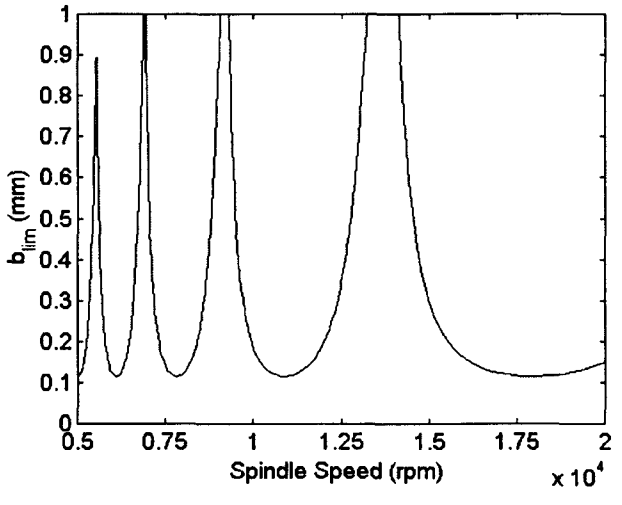

Figure 11: Stability Lobe Diagram 9:1 Tool.

To further investigate the interaction of tool modes with holder/spindle modes, receptance coupling simulations were completed for 7:1 to 12:1 tools. The minimum real part of the FRF was recorded for each case and used to estimate the critical stability limit ($b_{critical}$) for Y direction slot milling in aluminum, according to Equation 9 [21]. In this equation, K_s is the specific cutting force for the work piece material (700×10^6 N/m^2 [31]), μ_y is the 'average' direction orientation factor of the cutting force (cos 70° [31]), and z is the number of cutter teeth (2). The predicted slotting critical stability limits are plotted versus tool length in Figure 13. Increased stability is recognized at tool frequencies which correspond to holder/spindle modes (approximately 1344, 1114, 727, and 540.5 Hz). Although the expected general trend of decreasing stability for increasing tool length is seen, significant local increases in stability due to the 'dynamic absorber effect' are also recognized. The improved stability offered by the 727 Hz mode interaction (10:1 tool) agrees with the empirical machining results shown in [8].

$$b_{critical} = \frac{-1}{K_s \mu_y min(Re[G_{11}(\omega)])z} \quad (9)$$

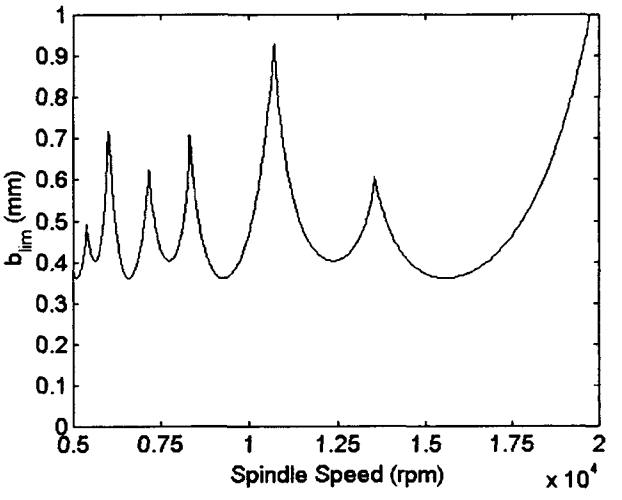

Figure 12: Stability Lobe Diagram 10:1 Tool.

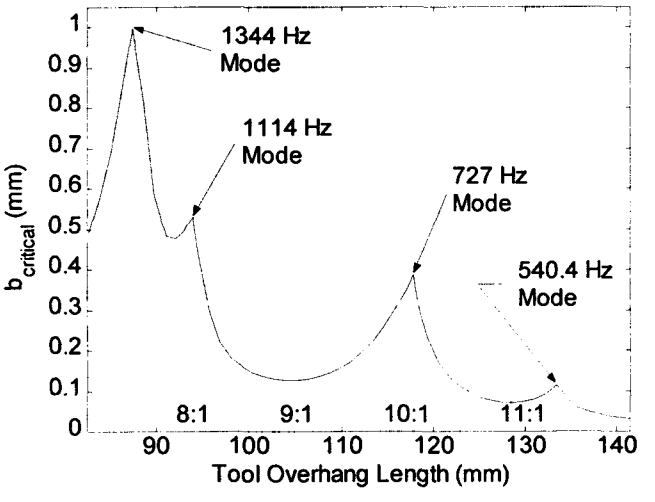

Figure 13: Critical Stability Limits vs. Tool Length.

6 CONCLUSIONS

The application of receptance coupling substructure analysis to tool point FRF prediction was demonstrated. It was shown that analytic expressions for tool FRFs could be coupled with holder/spindle experimental FRFs to predict the assembly's dynamic response.

A tool tuning example provided verification of this method. Experimental and predicted results showed dramatic variations in the tool point response as tool modes interacted with holder/spindle modes, similar to the effect seen in dynamic absorbers. Predicted local increases in the critical stability limit matched previous empirical results. Stability lobe diagrams were also generated and it was shown that two optimization criteria for proper tool length may be selected: 1) maximize the critical stability limit, and 2) maximize the chatter free axial depth of cut at the top available spindle speed.

7 ACKNOWLEDGEMENTS

The authors gratefully acknowledge support from The Boeing Company (Amy Helvey, St. Louis, MO, USA) and an NRC/NIST Postdoctoral Research Fellowship (for T. L. Schmitz). They would also like to recognize M. A. Davies of NIST for invaluable contributions to this work and thank C. J. Evans, J. R. Pratt, and M. D. Kennedy of NIST for helpful suggestions.

8 REFERENCES

[1] Smith, S., Tlusty, J., 1992, Stabilizing Chatter by Automatic Spindle Speed Regulation, Annals of the CIRP, 41/1: 433-436.

[2] Tlusty, J., Smith, S., Winfough, W., 1996, Techniques for the Use of Long Slender End Mills in High-Speed Machining, Annals of the CIRP, 45/1: 393-396.

[3] Smith, S., Tlusty, J., 1990, Update on High-Speed Milling Dynamics, Transactions of the ASME Journal of Engineering for Industry, 112: 142-149.

[4] Davies, M., Balachandran, B., 1996, Impact Dynamics in the Milling of Thin-Walled Structures, ASME Nonlinear Dynamics and Controls, DE-Vol. 91, 67-72.

[5] Agapiou, J., Rivin, E., Xie, C., 1995, Toolholder/Spindle Interfaces for CNC Machine Tools, Annals of the CIRP, 44/1: 383-387.

[6] Schultz, H., Moriwaki, T., 1992, High-Speed Machining, Annals of the CIRP, 41/2: 637-643.

[7] Heisel, U., Gringel, M., 1996, Machine Tool Design Requirements for High-Speed Machining, Annals of the CIRP, 45/1: 389-392.

[8] Davies, M., Dutterer, B., Pratt, J., Schaut, A., 1998, On the Dynamics of High-Speed Milling with Long, Slender Endmills, Annals of the CIRP, 47/1: 55-60.

[9] Winfough, W., Smith, S., 1995, Automatic Selection of the Optimum Metal Removal Conditions for High-Speed Milling, Transactions of the NAMRI/SME, 23: 163-168.

[10] Weck, M., Schubert, I., 1994, New Interface Machine/Tool: Hollow Shank, Annals of the CIRP, 43/1: 345-348.

[11] Weck, M., Hennes, N., Krell, M., 1999, Spindle and Toolsystems with High Damping, Annals of the CIRP, 48/1: 297-302.

[12] Delio, T., Tlusty, J., Smith, S., 1992, Use of Audio Signals for Chatter Detection and Control, Transactions of the ASME Journal of Engineering for Industry, 114: 146-157.

[13] Smith, S., Tlusty, J., 1991, An Overview of Modeling and Simulation of the Milling Process, Transactions of the ASME Journal of Engineering for Industry, 113: 169-175.

[14] Tlusty, J., Zaton, W., Ismail, F., 1983, Stability Lobes in Milling, Annals of the CIRP, 32/1: 309-313.

[15] Altintas, Y., Budak, E., 1995, Analytical Prediction of Stability Lobes in Milling, Annals of the CIRP, 44/1: 357-362.

[16] Tlusty, J., Ismail, F., 1981, Basic Non-linearity in Machining Chatter, Annals of the CIRP, 30/1: 299-304.

[17] Koenisberger, F., Tlusty, J., 1967, Machine Tool Structures-Vol. I: Stability Against Chatter, Pergamon Press.

[18] Tobias, S., 1965, Machine Tool Vibration, Blackie and Sons, Ltd.

[19] Merrit, H., 1965, Theory of Self-Excited Machine Tool Chatter, Transaction of the ASME Journal of Engineering for Industry, 87: 447-454.

[20] Minis, I., Yanushevsky, T., Tembo, R., Hocken, R., 1990, Analysis of Linear and Nonlinear Chatter in Milling, Annals of the CIRP, 39: 459-462.

[21] Tlusty, J., Smith, S., Zamudio, C., 1991, Evaluation of Cutting Performance of Machining Centers, Annals of the CIRP, 40/1: 405-410.

[22] Ewins, D., 1995, Modal Testing: Theory and Practice, Research Studies Press, Ltd., Somerset, England.

[23] Smith, S., Jacobs, T., Halley, J., 1999, The Effect of Drawbar Force on Metal Removal Rate in Milling, Annals of the CIRP, 48/1: 293-296.

[24] Ferreira, J., Ewins, D., 1995, Nonlinear Receptance Coupling Approach Based on Describing Functions, Proceeding of the 14th International Modal Analysis Conference, Dearborn, MI, 1034-1040.

[25] Ferreira, J., 1996, Transfer Report on Research Dynamic Response Analysis of Structures with Nonlinear Components, Internal Report- Dynamics Section, Imperial College, London, UK.

[26] Ren, Y., Beards, C., 1993, A Generalized Receptance Coupling Technique, Proceedings of the 11th International Modal Analysis Conference, Kissimmee, FL, 868-871.

[27] Klosterman, A., McClelland, W., Sherlock, I., 1977, Dynamic Simulation of Complex Systems Utilizing Experimental and Analytical Techniques, ASME, 75-WA/Aero-9.

[28] Thomson, W., Dahleh, M., 1998, Theory of Vibration with Applications 5th Ed., Prentice-Hall, Upper Saddle River, NJ.

[29] Blevins, R., 1979, Formulas for Natural Frequency and Mode Shape, Van Nostrand Reinhold Co., New York, NY.

[30] Tlusty, J., Ismail, F., 1990, Dynamic Structural Identification Tasks and Methods, Annals of the CIRP, 29/1: 251-255.

[31] Tlusty, J., 1985, Dynamics of High-Speed Milling, Handbook of High-Speed Machining Technology, R. I. King, ed., Chapman and Hall, New York, 48-153.

[32] Smith, S., Winfough, W., Halley, J., 1998, The Effect of Tool Length on Stable Metal Removal Rate in High-Speed Milling, Annals of the CIRP, 47/1: 307-310.